The Mount Meron infrasound array

An infrasound array without a noise reduction system

Averbuch, Gil; Ben-Horin, Yochai; Smets, Pieter S.M.; Evers, Läslo G.

DOI
10.1093/gji/ggz350

Publication date
2019

Document Version
Final published version

Published in
Geophysical Journal International

Citation (APA)
Averbuch, G., Ben-Horin, Y., Smets, P. S. M., & Evers, L. G. (2019). The Mount Meron infrasound array: An infrasound array without a noise reduction system. *Geophysical Journal International*, *219*(2), 1109-1117. https://doi.org/10.1093/gji/ggz350

Geophysical Journal International

Geophys. J. Int. (2019) **219,** 1109–1117
Advance Access publication 2019 July 30
GJI Seismology

doi: 10.1093/gji/ggz350

The Mount Meron infrasound array: an infrasound array without a noise reduction system

Gil Averbuch [1,2] Yochai Ben-Horin [3] Pieter S. M. Smets [1,2] and Läslo G. Evers [1,2]

[1] *Department of Geoscience and Engineering, Faculty of Civil Engineering and Geosciences, Delft University of Technology, 2628 CN, Delft, the Netherlands. E-mail: g.averbuch@tudelft.nl*
[2] *R&D Department of Seismology and Acoustics, Royal Netherlands Meteorological Institute, 3731 GA, De Bilt, the Netherlands*
[3] *Soreq Nuclear Research Center, National Data Center, Yavne* 818000, *Israel*

Accepted 2019 July 31. Received 2019 January 24; in original form 2019 July 1

SUMMARY

Measurements of seismo-acoustic events by collocated seismic and infrasound arrays allow for studying the two wavefields that were produced by the same event. However, some of the scientific and technical constraints on the building of the two technologies are different and may be contradicting. For the case of a new station, an optimal design that will satisfy the constraints of the two technologies can be found. However, in the case of upgrading an existing array by adding the complementing technology, the situation is different. The site location, the array configuration and physical constraints are fixed and may not be optimal for the complementing technology, which may lead to rejection of the upgrade. The International Monitoring System (IMS) for the verification of the Comprehensive Nuclear-Test-Ban Treaty (CTBT) includes 37 seismic arrays and 51 infrasound arrays. Although the CTBT verification regime is fixed in the treaty, an upgrade of the existing arrays by adding more technologies is possible.

The Mount Meron seismic array (MMAI), which is part of the IMS, is composed of 16 sites. Microbarometers were installed at five MMAI sites to form the Mount Meron infrasound array. Due to regulation and physical constraints, it was not possible to relocate the sites nor to install analogue noise reduction filters (i.e. a pipe array). In this study, it is demonstrated that the installation of the MMAI infrasound array is beneficial despite the non-optimal conditions. It is shown that the noise levels of the individual array sites are between the high and median global noise levels. However, we claim that the more indicative measures are the noise levels of the beams of interest, as demonstrated by analysing the microbaroms originated from the Mediterranean Sea. Moreover, the ability to detect events relevant to the CTBT is demonstrated by analysing man-made events during 2011 from the Libya region.

Key words: Infrasound; Instrumental noise; Spatial analysis; Tides and planetary waves; Time-series analysis.

1 INTRODUCTION

Infrasound consists of low-frequency acoustic signals that propagate in the atmosphere. Detection of infrasonic signals is used as a monitoring technology for both natural and anthropogenic events. Examples of sources generating infrasonic signals include volcanic eruptions, earthquakes, explosions and ocean waves (Campus & Christie 2009). The ability of infrasound to efficiently propagate over long distances leads to its employment as one of four technologies that are used to detect and verify nuclear tests. Global monitoring in the atmosphere, solid earth and oceans for the verification of the Comprehensive Nuclear-Test-Ban Treaty (CTBT) is obtained by its International Monitoring System (IMS; Dahlman *et al.* 2009a). The IMS includes 37 seismic arrays and 51 ground-based infrasound arrays that are certified and sending data real-time to the International Data Center in Vienna (status in June 2019).

Infrasound detections are made by arrays of three or more microbarometers. The usage of arrays allows us to enhance the signal-to-noise ratio (SNR), and therefore improves the detection capability. Moreover, different array processing methods provide us with the directionality of the detected signal (e.g. Melton & Bailey 1957; Rost & Thomas 2002). In theory, the detection potential of an array and its ability to resolve the wave parameters depend on the array configuration and the signal of interest (the wavelength should be within the same order of the array aperture). In practice, the level

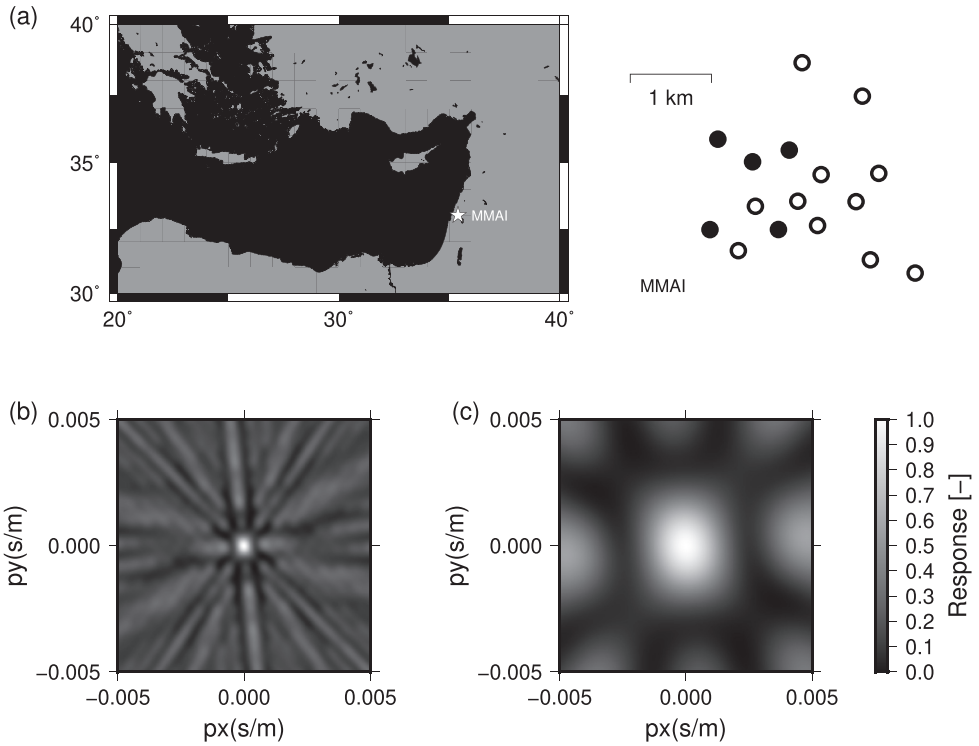

Figure 1. (a) Location and layout of MMAI seismo-acoustic array. The five array elements with an infrasound sensor are indicated by the solid black circles. Array response of the five infrasound elements for (b) 0.5–1.5 Hz and (c) 0.15–0.25 Hz.

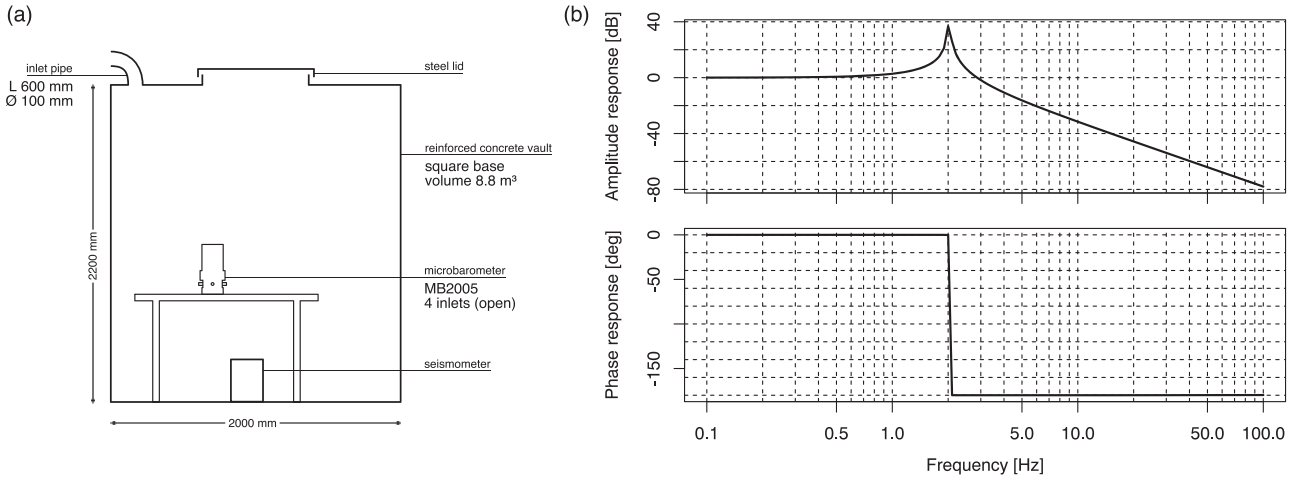

Figure 2. (a) Vault schematic and sensor location. (b) Theoretical response of the vault and inlet pipe assuming that it behaves like an idealized Helmholtz resonator.

of local anthropogenic and wind noise plays a significant role in detection performance. Therefore, wind noise reduction systems are essential (Hedlin & Raspet 2003).

The growing interest in seismo-acoustic events entails that collocated infrasound and seismic arrays are beneficial (Shani-Kadmiel *et al.* 2018). The two technologies are complementary and measure different propagation paths of the seismo-acoustic wavefield produced by an event. Thus the observable seismic and acoustic signals are independent and enable improving the source identification. Due to the different nature of seismic and infrasonic signals, a design of a collocated array must satisfy the requirements of both techniques. Moreover, upgrading an existing array by adding new instruments may lead to a non-optimal configuration for the new technology.

Here, the IMS Mount Meron seismic array is used as a case study. The array is composed of 16 elements with minimal interdistance of 350 m and an aperture of approximately 2 km. All elements' installation is planned to have a low surface signature as the array is located in an agricultural area on the border of a national nature reserve. During 2010 it was decided to build a new infrasound array in the northern part of Israel. The motivation to prefer an upgrade to MMAI instead of building a new array was driven equally by the scientific gain from collocated arrays and the expected lower costs for upgrading as the infrastructure was already in place. These were the primary decisive considerations despite the plausible non-optimal configuration, as well as the understanding that due to the low signature constraint, no mechanical wind reduction system could be

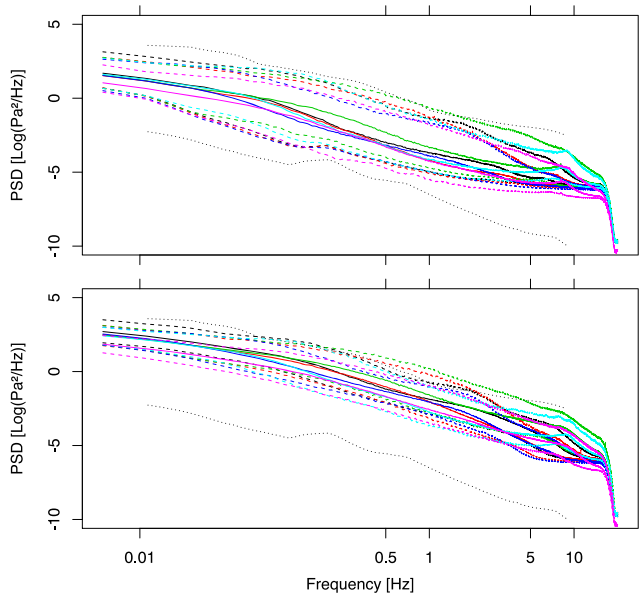

Figure 3. Yearly average PSD estimated at (top) 3 UTC and (bottom) 9 UTC. The 5 per cent (dashed), 50 per cent (solid) and 95 per cent (dashed) are presented for each array site: IMA1 (black), IMA2 (red), IMA3 (green), IMA4 (blue), IMA5 (cyan) as well as the incoherent beam (magenta). High and low global noise levels are given by dotted black lines.

used. MMAI infrasound array performance is assessed in order to demonstrate that despite the hard constraints, the array can be used for both scientific and operational purposes.

Section 2 describes the array properties and its theoretical detection capability. Analysis of the noise levels is presented in Section 3. It is shown that the noise levels at the array elements lie between the median and high global noise model (Brown *et al.* 2014; McNamara & Buland 2004; Bowman *et al.* 2005). Section 4 shows the detection capabilities of the array. Despite the above average noise levels, continuous low-frequency signals from Mediterranean microbaroms are detected. Furthermore, the augmentation of the array to the CTBT purpose is demonstrated by the analysis of long-range explosions that occurred in Libya during 2011. Doing so, both the ambient noise field and deterministic transient signals are evaluated in order to show the performance of the array. Throughout the paper, all the times correspond to UTC. The local time is GMT+2.

2 ARRAY DESCRIPTION

The MMAI seismic array is located in the north of Israel in a valley (average elevation of 800 m) near Mount Meron (elevation 1208 m), between the Mediterranean Sea (approximately 25 km to the west of the array) and the Sea of Galilee (approximately 20 km southeast of the array) (Fig. 1). The array is composed of 16 elements with a minimal distance between the sites of 350 m and an aperture of approximately 2 km. The array sites receive the electric power, communication and GPS from the Central Recording Facilities (CRF) located at Kibbutz Sasa, the data are transmitted to the Israel National Data Center (NDC). An upgrade can be done by declaring the new part as a Cooperating National Facility (CNF) or as a National Technical Means (NTM), as defined by the CTBT (Dahlman *et al.* 2009b). CNF is a group of stations compliant with all IMS specifications but operated by the state and not part of the IMS network. However, these stations can be used in a similar way as the IMS stations in the case of a suspicious event. NTM is any added technology operated by the state that does not satisfy the IMS requirements. These technologies will unlikely be used for treaty verification.

Five MMAI sites (Fig. 1b) were chosen by the Israel NDC to serve as sites for the infrasound array elements part of an NTM. The elevation of four of the sites is approximately 810 m, and one site is located at an elevation of 892 m. Each site includes an MB2005 microbarometer and a Quanterra q330 digitizer with local GPS antenna. The data are collected on a computer at the CRF and from there transmitted to the NDC. Due to environmental constraints, it is impossible to introduce a wind reduction system. The instruments are placed on a table in the seismic vaults as described schematically in Fig. 2(a). Fig. 2(b) presents the theoretical response function of the vault, assuming that the vault behaves like an idealized Helmholtz resonator, that is, the combination of a volume and a pipe. Resonance within the pipe upon flow excitation is predicted at approximately 2 Hz. However, when the mean flow is of a very low Mach number and the resonator diameter is small, the velocity in the pipe can become too large. Hence, turbulence increases the flow resistance prevailing flow excitation and so resonance to occur (Dowling & Hughes 1992; Tang 2010). Moreover, the sensor is positioned within the cavity away from the resonating pipe. Therefore, the actual resonance effect is expected to be less pronounced than represented in Fig. 2(b). The effect of small differences between the vaults on the response functions are negligible and should not affect the array analysis.

The finite aperture of the array and interdistances between the elements lead to limited spatial sampling of the wavefield. Therefore, its reconstruction by any array processing method is restricted by the array response. Two frequency bands are used for the theoretical array response. (1) 0.5–1.5 Hz for the long-range transient signals. (2) 0.15–0.25 Hz that represents the microbaroms' frequency range. Figs 1(b) and (c) show the MMAI infrasound array response for two frequency bands, from 0.5 to 1.5 Hz and from 0.15 to 0.25 Hz, respectively. Using lower frequencies than 0.15 Hz would have led to a larger main lobe, which decreases the ability to determine the wave parameters. Frequencies above 1.5 Hz lead to spatial aliasing, which increases the uncertainties of the resolved wavefield. The array layout manifests a slight non-uniform sensitivity: the sensitivity in the east–west direction is slightly higher (more focused) compared to the north–south direction.

3 NOISE ANALYSIS

Any station's noise level is temporal. In order to estimate the typical noise levels, the hourly noise level is estimated four times per day, at 3, 9, 15 and 21 UTC, for each of the array elements and the incoherent array beam, which is the sum of the unshifted recordings. A sliding window of 3 min with 68 per cent overlap and Nuttall tapering is applied to the data from 2016 (Welch 1967; McNamara & Buland 2004; Brown *et al.* 2014). Noise levels are estimated using procedures developed in the Python environment using ObsPy, SciPy and NumPy toolboxes (Jones *et al.* 2001; Oliphant 2006; Beyreuther *et al.* 2010); statistical analysis of the noise segments is done using R statistical computing (R Core Team 2013). High noise levels of some elements exceed the global high noise model (dashed lines) due to the lack of a wind noise reduction system. However, the noise levels of the incoherent beam (magenta) are always below

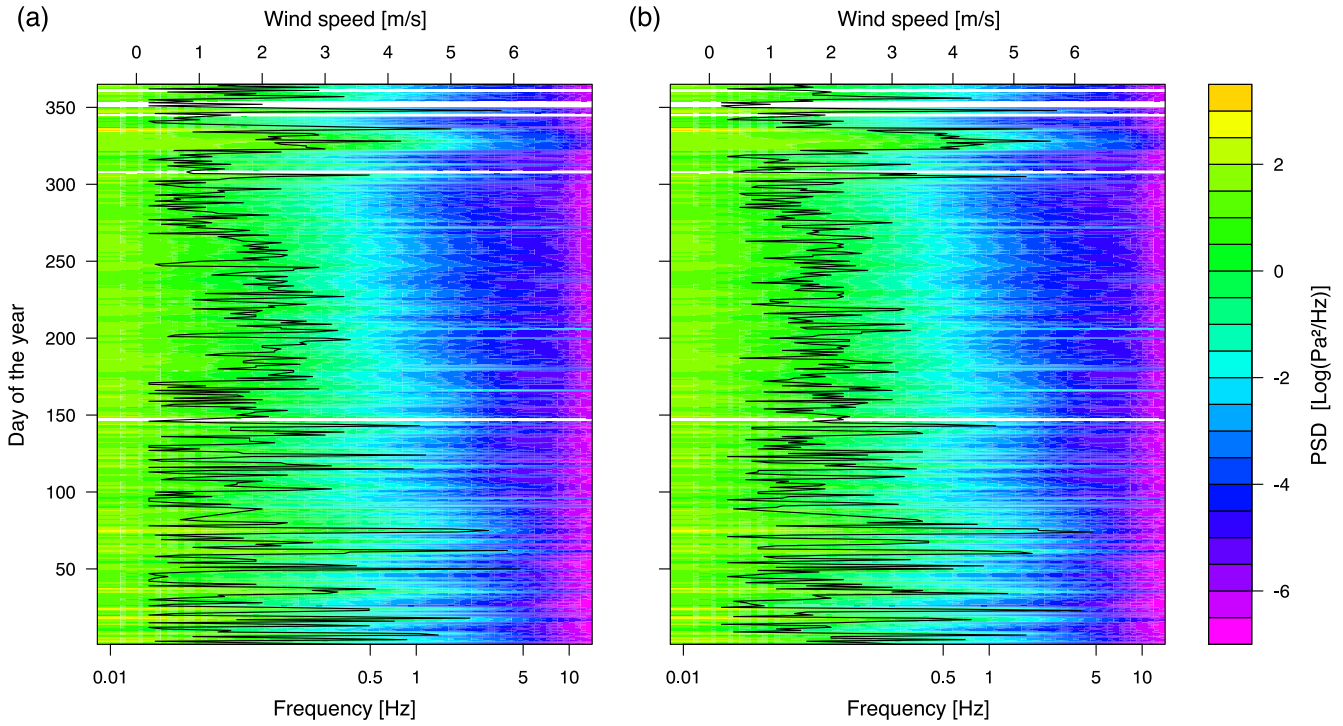

Figure 4. Averaged PSD levels of the incoherent beam and wind velocity (black lines) at (a) 3 and (b) 9 UTC during 2016. Days with higher wind velocity correspond to days with higher noise levels.

it. Noise can be suppressed by summation due to its incoherency between the sites. Hence, array beams are used in the analysis rather than single elements to improve the SNR.

Fig. 3 shows the yearly average power spectral density (PSD), at 3 and 9 UTC, of the five array elements and the incoherent array beam. At 3 UTC, the average noise levels (solid lines) are located at the centre of the region between the low and high global noise levels (black dotted lines). Similar results were obtained for 15 and 21 UTC. At 9 UTC, the average noise levels are higher and closer to the high global noise model. During the day, when the noise levels are higher, only higher SNR signals can be detected. The 5 and 95 noise levels percentiles (dashed lines) show an increase in the PSD between 0.1 and 0.3 Hz (peaking around 0.2 Hz) at 3, 15 and 21 UTC (only 3 UTC is shown). Therefore, microbaroms can be detected at these time slots. Furthermore, we can conclude that the incoherent beam performs similar as the individual elements and thus can represent the characteristic average noise level of the array.

The dependency of the incoherent beam average PSD levels on the time of the year is presented in Fig. 4, for 3 UTC (a) and 9 UTC (b) as representative of the best and worst time slots, respectively. In the proximity of the IMA4 site, there is a meteorological station operated by MIGAL Galilee Research Institute LTD (http://www.mop-zafon.net/). The wind is measured 2 m above the ground, and the presented values are a 1 hr average with a 0.1 m s^{-1} error. Winds measurements (black lines) show a pronounced effect on the noise. It can be seen from the correlation between days with higher noise levels to days with high wind velocity. During summer, that is, July–October, the wind is more stable with higher average wind velocities of 2–3 m s^{-1}. In winter, the wind is more variable with peaks that can reach up to 7 m s^{-1}. Accordingly, noise levels are more contiguous but higher in summer while lower but more variable in winter.

Both Figs 3 and 4 do not indicate a significant signature of the Helmholtz resonator.

4 DATA ANALYSIS

The data are processed using a delay and sum beamforming. For a set of defined slowness parameters, a beam is formed and the Fisher ratio F is calculated. The slowness parameters with the highest F value characterize the most coherent wave to cross the array. The plane-wave backazimuth (BA) and apparent velocity (AV), which correspond to a slowness vector, can be calculated from the slowness parameters (Melton & Bailey 1957; Evers 2008). For each time segment, F is calculated as follows:

$$F = \frac{T(N-1)\sum_{t=1}^{T}(\sum_{n=1}^{N} x_{nt})^2 - \frac{1}{T}(\sum_{t=1}^{T}\sum_{n=1}^{N} x_{nt})^2}{N(T-1)\sum_{t=1}^{T}\sum_{n=1}^{N} x_{nt}^2 - \frac{1}{N}\sum_{t=1}^{T}(\sum_{n=1}^{N} x_{nt})^2}, \quad (1)$$

where N and T are the number of elements and samples, respectively. x_{nt} is the time-delayed sample of sensor n and time sample t, assuming a trialled BA and AV. This procedure provides a time-series with Fs, BAs and AVs (which correspond to a slowness vector). The SNR of a recorded channel can be calculated by $F = N \cdot \mathrm{SNR}^2 + 1$.

Detection can be defined in several ways. For automatic detections, a threshold SNR or Fisher ratio can be defined. These values can be approximated by the theoretical central and non-central Fisher distributions (Evers 2008) or by statistical studies (Le Pichon *et al.* 2009b). A short-time average over long-time average (STA/LTA) can be applied on the recording or on the beamforming results in order to extract events from the background noise (Mitchell *et al.* 1998; Evers & Snellen 2015). Moreover, constant BA values can be an indicator for a real event (Brown *et al.* 2008;

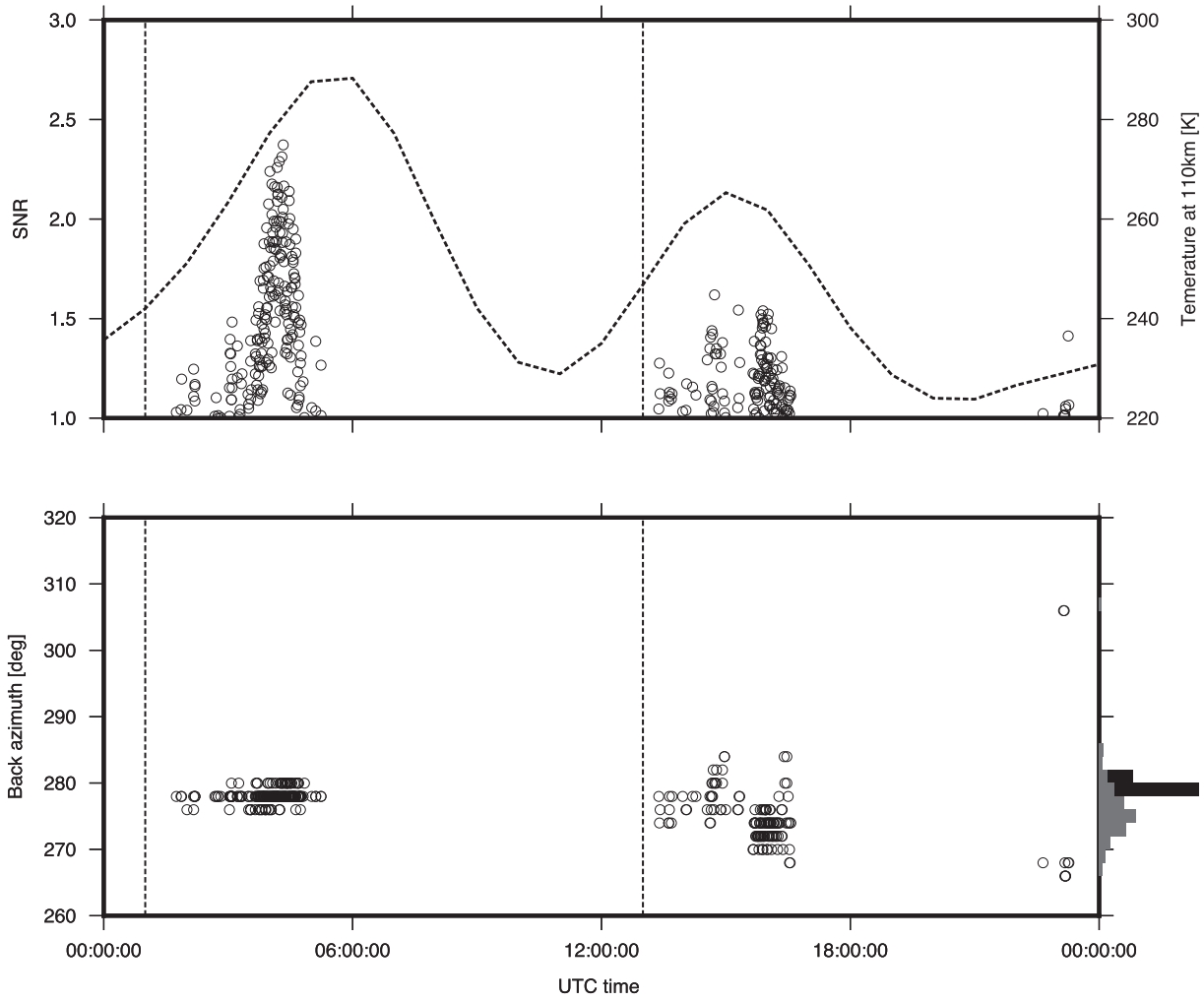

Figure 5. Microbarom detections on 2013 May 29, with SNR $\geq$ 1 from MMAI. The top frame shows the variation of the SNR and temperature at 110 km (horizontal dashed line). Bottom frame shows the BA detections. The distributions of detections at MMAI in the morning and afternoon are shown in black and dark grey, respectively. Vertical dashed lines at 01:00 and 13:00 highlight the 12-hr semi-diurnal cycle in the detections. This cycle suggests on a thermospheric propagation, which is affected by semi-diurnal solar tides in the thermosphere.

Averbuch *et al.* 2018). The array performance will be demonstrated by detecting two types of signals: continuous low-frequency signals from Mediterranean microbaroms and infrasonic deterministic transient signals from long-range explosions.

4.1 Continuous signals: Mediterranean microbarom analysis

Microbaroms are pressure perturbations in the atmosphere caused by the nonlinear interaction of oceanic surface waves. When the interaction forms a standing wave, the oscillation of the water–air interface radiates acoustic energy into the ocean and atmosphere. Large microbarom source regions corresponding to the deep ocean, that is, North Atlantic Ocean, typically dominate the infrasound ambient noise field characterized by a radiation frequency of 0.2 $\pm$ 0.1 Hz (Le Pichon *et al.* 2009a; Smets & Evers 2014). The Mediterranean allows microbaroms with frequencies up to 1 Hz due to shallower depths (Assink *et al.* 2014). In winter, stratospheric propagation from the Atlantic Ocean towards the Israeli infrasound arrays is favourable due to the eastward stratospheric circumpolar vortex. Consequentially, distant deep Atlantic Ocean microbaroms usually mask the less energetic Mediterranean signals. During summer, the stratospheric wind is characterized by a westward vortex that prevents long-range stratospheric propagation from the Atlantic Ocean. Moreover, thermospheric propagation is not likely for distances over 4000 km (Smets & Evers 2014). Therefore, summertime Mediterranean microbaroms are detectable by MMAI without being masked by energetic microbaroms from the Atlantic Ocean.

Infrasound data from May and July 2013 are bandpass filtered between 0.1 and 1 Hz and beamformed according to Section 4 with the parameters from Table 1. Detections at MMAI suggest Mediterranean microbarom activity that is verified by microbarom modelling. Microbaroms are modelled including finite ocean depth effects (Waxler & Gilbert 2006; Waxler *et al.* 2007; Smets & Evers 2014). 2-D ocean surface wave spectra driving the microbarom model are obtained from the European Centre for Medium-Range Weather Forecasts operational high-resolution coupled ocean-atmosphere model (HRES-WAM) for the Mediterranean region.

Fig. 5 shows the beamforming results, with SNR $\geq$ 1, of MMAI array for 2013 May 29. The histogram next to the BA panel represents the distribution of the BA detections of the array for the first

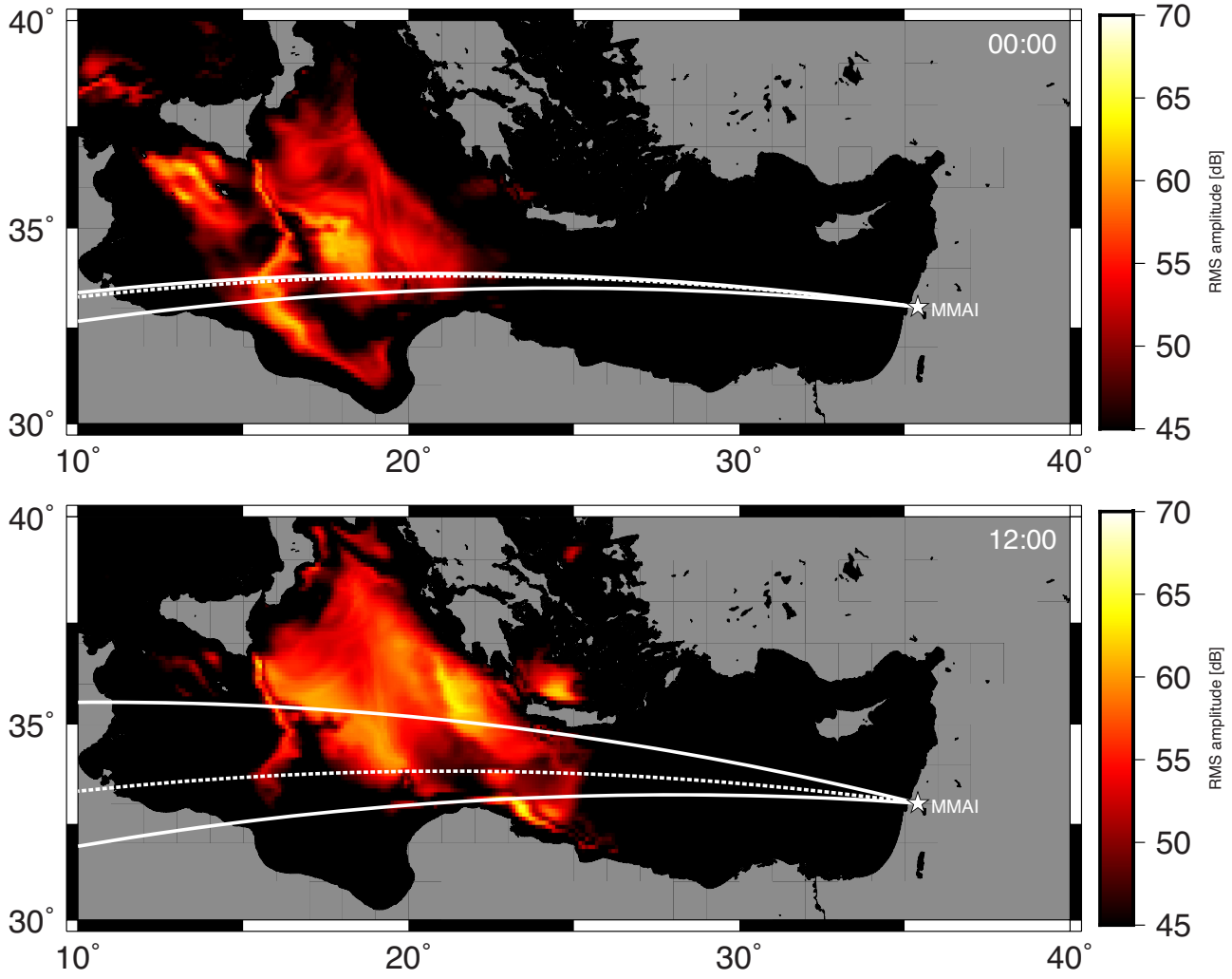

Figure 6. BA cones and microbarom modelling for the time segments 00:00 ±3 and 12:00 ±3 on 2013 May 29. White lines represent the BA cones of SNR ≥ 1 from MMAI. These lines correspond to the upper and lower BA detections with SNR ≥ 1. Colours represent the modelled microbaroms' RMS pressure amplitude.

and second halves of the day. In the morning, 00:00–12:00, MMAI detections are centred around 278°. These maxima correspond to the dashed lines in the upper frame of Fig. 6, which points to the centre of the microbarom area. In the afternoon, 12:00–24:00, MMAI detections are centred around 274°. All detections point toward the microbarom area (lower frame of Fig. 6).

Detections at MMAI start shortly after 01:45 up to 05:15 and appear again from 13:30 until 16:30. This semi-diurnal cycle suggests a thermospheric propagation. Semi-diurnal solar tides in the thermosphere lead to variations in the mesopause altitude and therefore in the thermosphere return height (Smets & Evers 2014). When return heights are low, there is less damping, and more energy propagates over long distances. The dashed line in Fig. 5 represents the temperature variations at an altitude of 110 km above MMAI. At 110 km the thermospheric temperature was equivalent or larger than the ground temperature, indicating the thermosphere waveguide altitude. Peaks in the temperature, which correspond to a lower return height, are consistent with the detections apex. Temperature is obtained from NRLMSISE-00 atmosphere model (Picone *et al.* 2002).

4.2 Detection of transient events

Explosions at two cities in Libya during 2011 March 28 are used to demonstrate the MMAI capability in detecting deterministic transient signals. (BBC 2011). The events' distance from MMAI is more than 2000 km. Data are bandpass filtered between 0.5 and 1.5 Hz and beamformed with the parameters listed in Table 2. The Late-Review-Bulletin (LEB) by the Comprehensive-Nuclear-Test-Ban Treaty Organization (CTBTO) is used to verify the detections. A theoretical BA and arrival time are calculated for each of the eight LEB events assuming a horizontal propagation velocity of 300 m s^{-1}, which typically corresponds to stratospheric propagation. Cross-winds are neglected for this first-order approximation. The events were detected by at least four of the IMS infrasound stations I48TN (Tunisia), I26DE (Germany), I43RU (Russia), I17CI (Ivory Coast), I31KZ (Kazakhstan) and I32KE (Kenya). These stations provide azimuthal coverage for events in the Mediterranean region, between southeast and northeast clockwise from north. A semi-empirical detection capability of the IMS network predicts a low detection potential for events in the Mediterranean region for that time of the year (Tailpied *et al.* 2017; Le Pichon *et al.*

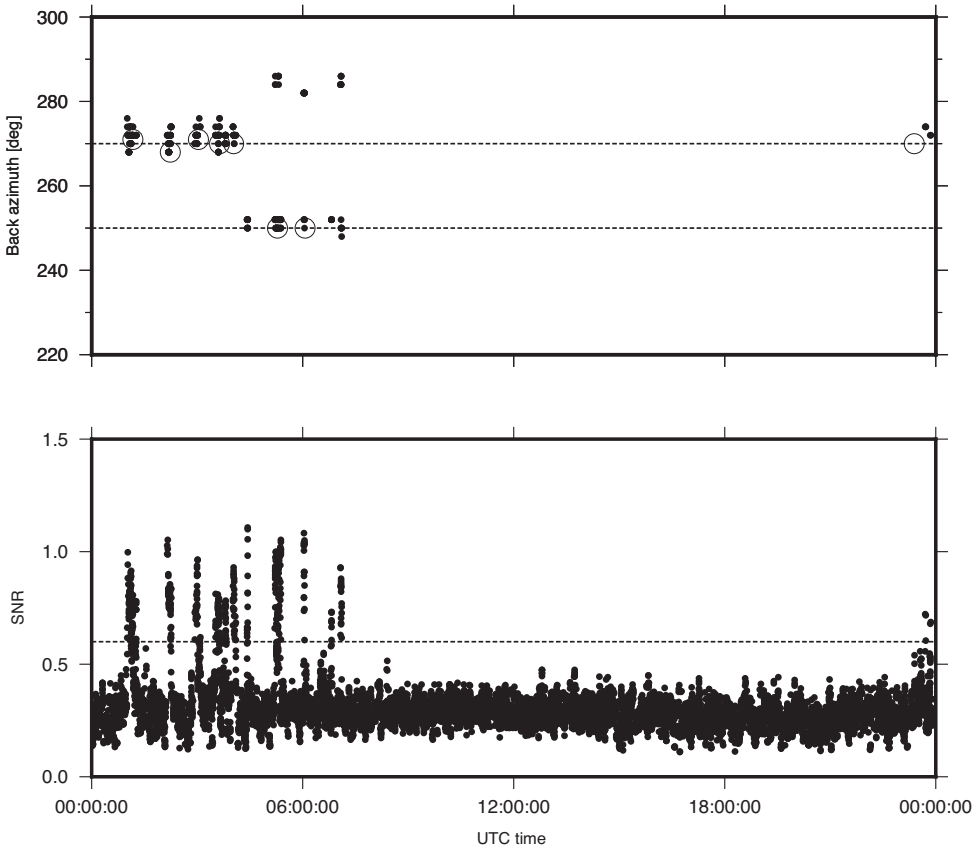

Figure 7. Array processing results of 2011 March 28 with apparent velocity ≥ 300 m s^{-1}. Bottom: SNR with detection threshold SNR ≥ 0.6 (dashed line). Top: backazimuth of the detections (black dots). Eight Libya events of the LEB represented by the true bearing and an expected arrival time assuming stratospheric propagation (circles). The dashed lines indicate the backazimuth of the two sites of the explosions.

Table 1. Beamforming parameters for the microbarom detections.

	Bin size	Overlap	BA range	BA intervals	AV range	AV intervals
MMAI	51.2 s	50 per cent	260–300°	2°	250–450 m s^{-1}	5 m s^{-1}

Table 2. Beamforming parameters for the Libyan transient event detections.

	Bin size	overlap	BA range	BA intervals	AV range	AV intervals
MMAI	51.2 s	90 per cent	0–360°	2°	250–450 m s^{-1}	5 m s^{-1}

2019). Therefore, MMAI infrasound station can improve the IMS capabilities by filling a large coverage gap in the east part of the Mediterranean.

Fig. 7 shows the analysis results of 2011 March 28. The mean SNR value for that day is 0.3, and a detection threshold value is defined to be SNR $\geq$ 0.6. Black circles indicate the true BA and expected arrival time of the LEB events, assuming stratospheric propagation and no cross-wind. Most of the BA results are aligned with the true BA of the events' location. Multiple detections can be associated with a similar event as these detections correspond to a different part of the same wave train. Discrepancies between the detections and events in Fig. 7 can be attributed to the limitations of the first-order propagation approximation. Detections that do not correspond to the LEB can be explained by (1) missed events and (2) false alarms. Missed events can be explained by either a local event or an event that was not picked up by a minimum number of three IMS stations.

5 SUMMARY AND DISCUSSION

The Mount Meron collocated seismo-acoustic array is an example of a seismic array that was upgraded by adding infrasound components to five of the existing vaults. The decision to use the existing infrastructure dictated the possible array configuration, which is not optimal for an infrasound array. Moreover, due to environmental constraints, no mechanical wind noise reduction system was installed, and the microbarometers are placed in the seismic vault. Thus, this study was devoted to assessing the detection capabilities of the array. The methods of evaluation are based on the following:

(i) Estimating the average noise levels of the individual elements and the incoherent beam.

(ii) Detection of continuous signals, that is, Mediterranean microbaroms.

(iii) Detection of long-range transient signals and comparing them to events as listed by the CTBTO.

The noise levels were estimated, following the work by Brown *et al.* (2014), for four representative times of the day. It is demonstrated that for three time slots (3, 15 and 21 hr UTC), the average noise levels of the individual array elements and the incoherent beam were within the global low and high noise model (Brown *et al.* 2014). These time slots correspond to the middle of the night, late afternoon and evening, which are known to be less noisy. However, for the time slot of 9 UTC (local noon time), the noise levels were comparable to the high global noise model. Moreover, it was demonstrated that there is a good correlation between periods of the year with high noise levels to periods which are associated with high winds. No significant signature that the vault behaves like a Helmholtz resonator is observed.

Two data sets were analysed in order to demonstrate the MMAI detection capability. Detections of Mediterranean microbaroms showed the array potential in identifying low-frequency signals. The semi-diurnal cycle in the observations corresponds to thermospheric tides, which influence the infrasound return height. A decrease in thermospheric temperatures increases the return height, resulting in extended propagation through a dispersive, attenuating media. Therefore, less coherent energy arrives at the array. Moreover, there is a good agreement between the detectionless period in Fig. 5 and the noisy time slot of 9 UTC. The explosions in Libya are used to assess its performance in detecting long-range deterministic transient signals during low noise conditions. All the events from the LEB catalogue were detected. Events that do not correspond to the catalogue can be either missed events or false alarms.

Based on the analysis presented in this work we conclude that despite the non-optimal installation, the array has an important contribution to monitoring infrasound from both the Mediterranean Sea, that is, ambient noise, and for detecting deterministic transient signals in the region. The latter will allow for the identification of sources of interest for CTBT verification. From a regional perspective, MMAI fills a large spatial coverage gap of the global IMS in the east part of the Mediterranean. It is not professed that the array is a top performance array, and that wind noise reduction systems are not of importance. If it was possible, the array would have been equipped with noise reduction systems. However, if one reflects on the added value of a non-optimal array, and faces the question of building one, the answer is yes. Nevertheless, by calculating the noise levels at each element, the environmental characteristics of the array can be compared with those around the world, based on the high and low noise models. However, when judging the performance of an array, the noise at array beams is to be evaluated. Depending on the array configuration, that is, the number of elements, interelement distances, aperture and analogue noise reduction, an array in a moderate to high noise environment might have a good performance as shown in this study.

ACKNOWLEDGEMENTS

All the data were obtained by the Israel National Data Center. The meteorological station is operated by Dr. Joseph Tsipris and Dr. Moshe Meron. GA is funded through the Marie Curie Action WAVES from the European Union within H2020, Grant Number 641943. The contribution of PSMS and LGE are funded through a VIDI project from the Netherlands Organization for Scientific Research (NWO), Project 864.14.005. The authors are grateful for helpful reviews by the editor, and the anonymous reviewers.

REFERENCES

Assink, J. D., Waxler, R., Smets, P. & Evers, L.G., 2014. Bidirectional infrasonic ducts associated with sudden stratospheric warming events, *J. geophys. Res.,* **119**(3), 1140–1153.

Averbuch, G., Assink, J.D., Smets, P.S.M. & Evers, L.G., 2018. Extracting low signal-to-noise ratio events with the Hough transform from sparse array data, *Geophysics,* **83**(3), WC43–WC51.

BBC, 2011. Libya: UK and France urge supporters to drop Gaddafi, https://www.bbc.com/news/uk-12879482.

Beyreuther, M., Barsch, R., Krischer, L., Megies, T., Behr, Y. & Wassermann, J., 2010. Obspy: a python toolbox for seismology, *Seismol. Res. Lett.,* **81**(3), 530–533.

Bowman, J.R., Baker, G.E. & Bahavar, M., 2005. Ambient infrasound noise, *Geophys. Res. Lett.,* **32**(9), L09803.

Brown, D., Ceranna, L., Prior, M., Mialle, P. & Le Bras, R.J., 2014. The IDC seismic, hydroacoustic and infrasound global low and high noise models, *Pure appl. Geophys.,* **171**(3-5), 361–375.

Brown, D.J., Whitaker, R., Kennett, B. L.N. & Tarlowski, C., 2008. Automatic infrasonic signal detection using the Hough transform, *J. geophys. Res.,* **113**(D17), D17105.

Campus, P. & Christie, D.R., 2009. Worldwide observations of infrasonic waves, in *Infrasound Monitoring for Atmospheric Studies,* pp. 185–234, eds Le, Pichon A., Blanc, E. & Hauchecorne, A. , Springer Netherlands.

Dahlman, O., Mykkeltveit, S. & Haak, H., 2009a. Monitoring technologies, in *Nuclear Test Ban,* chap. 2, pp. 25–58, Springer Netherlands.

Dahlman, O., Mykkeltveit, S. & Haak, H., 2009b. The treaty, in *Nuclear Test Ban,* chap. 4, pp. 83–98, Springer Netherlands.

Dowling, A. & Hughes, I., 1992. Sound absorption by a screen with a regular array of slits, *J. Sound Vib.,* **156**(3), 387–405.

Evers, L.G., 2008. The inaudible symphony: on the detection and source identification of atmospheric infrasound, *PhD thesis,* TU Delft, Delft University of Technology.

Evers, L.G. & Snellen, M., 2015. Passive probing of the sound fixing and ranging channel with hydro-acoustic observations from ridge earthquakes, *J. acoust. Soc. Am.,* **137**(4), 2124–2136.

Hedlin, M.A.H. & Raspet, R., 2003. Infrasonic wind-noise reduction by barriers and spatial filters, *J. acoust. Soc. Am.,* **114**(3), 1379–1386.

Jones, E., Oliphant, T. & Peterson, P., 2001. *SciPy: Open Source Scientific Tools for Python,* http://www.scipy.org/.

Le Pichon, A., Blanc, E. & Hauchecorne, A., 2009a. *Infrasound Monitoring for Atmospheric Studies,* Springer Netherlands.

Le Pichon, A., Vergoz, J., Blanc, E., Guilbert, J., Ceranna, L., Evers, L. & Brächet, N., 2009b. Assessing the performance of the International Monitoring System's infrasound network: geographical coverage and temporal variabilities, *J. geophys. Res.,* **114**(8), 25–28.

Le Pichon, A., Ceranna, L., Vergoz, J. & Tailpied, D., 2019. Modeling the detection capability of the global IMS infrasound network, in *Infrasound Monitoring for Atmospheric Studies,* chap. 17, pp. 593–604, Le, Pichon A., Blanc, E. & Hauchecorne, A., Springer International Publishing, .

McNamara, D.E. & Buland, R.P., 2004. Ambient noise levels in the continental united states, *Bull. seism. Soc. Am.,* **94**(4), 1517–1527.

Melton, B.S. & Bailey, L.F., 1957. Multiple signal correlators, *Geophysics,* **22**(3), 565.

Mitchell, M., Aster, R., Young, C., Beiriger, J., Harris, M., Moore, S. & Trujillo, J., 1998, A comparison of select trigger algorithms for automated global seismic phase and event detection. *Bull. seism. Soc. Am.,* **88,** 95–106.

Oliphant, T.E., 2006. *A Guide to NumPy,* Trelgol Publishing.

Picone, J., Hedin, A., Drob, D.P. & Aikin, A., 2002. NRLMSISE-00 empirical model of the atmosphere: statistical comparisons and scientific issues, *J. geophys. Res.,* **107**(A12), SIA 15–1-SIA 15-16.

R Core Team, 2013. *R: A Language and Environment for Statistical Computing,* R Foundation for Statistical Computing.

Rost, S. & Thomas, C., 2002. Array seismology: methods and applications, *Rev. Geophys.,* **40**(3), 2–1-2-27.

Shani-Kadmiel, S., Assink, J.D., Smets, P. S.M. & Evers, L.G., 2018. Seismoacoustic coupled signals from earthquakes in Central Italy: epicentral and secondary sources of infrasound, *Geophys. Res. Lett.,* **45**(1), 427–435.

Smets, P.S. & Evers, L.G., 2014. The life cycle of a sudden stratospheric warming from infrasonic ambient noise observations, *J. geophys. Res.,* **119**(21), 12 084–12 099.

Tailpied, D., Le Pichon, A., Marchetti, E., Assink, J. & Vergniolle, S., 2017. Assessing and optimizing the performance of infrasound networks to monitor volcanic eruptions, *Geophys. J. Int.,* **208**(1), 437–448.

Tang, S.K., 2010. On sound transmission loss across a Helmholtz resonator in a low Mach number flow duct, *J. acoust. Soc. Am.,* **127**(6), 3519–3525.

Waxler, R. & Gilbert, K.E., 2006. The radiation of atmospheric microbaroms by ocean waves, *J. acoust. Soc. Am.,* **119**(5), 2651–2664.

Waxler, R., Gilbert, K., Talmadge, C. & Hetzer, C., 2007. The effects of the finite depth of the ocean on microbarom signals, in *8th International Conference on Theoretical and Computational Acoustics (ICTCA),* European Acoustics Association (EAA), Crete, Greece.

Welch, P.D., 1967. The use of fast Fourier transform for the estimation of power spectra: a method based on time averaging over short, modified periodogram, *IEEE Trans. Audio Electroacoust.,* **15**(2), 70–73.